EDGE ARTICLE

Design of efficient thermally activated delayed fluorescence blue host for high performance solution-processed hybrid white organic light emitting diodes†

Xinxin Ban, [ID] *[ab] Feng Chen,[a] Yan Liu,[a] Jie Pan,[a] Aiyun Zhu,[a] Wei Jiang*[b] and Yueming Sun[b]

Developing a solution-processible blue thermally activated delayed fluorescence (TADF) emitter for hybrid white organic light emitting diodes (WOLEDs) is still a challenge. In this work, two TADF blue emitters are designed and synthesized to explore a common strategy to qualify the small molecular TADF material as a solution-processible blue host. Systematic studies find that the molecular encapsulation by introducing unconjugated carbazoles as steric shields not only keeps the intrinsic TADF feature unchanged, but also effectively suppress the intermolecular interaction induced exciton quenching, which makes the material more efficient for solution-processing. The optimized solution-processed hybrid WOLEDs based on the encapsulated TADF blue host realized a highly efficient device performance with a maximum current efficiency (CE), power efficiency (PE) and external quantum efficiency (EQE) of 45.6 cd A^{-1}, 40.9 lm W^{-1} and 17.0%, respectively, which are three times higher in device efficiency and twenty times higher in device lifetime than the corresponding device with an unencapsulated TADF blue host. Furthermore, the obtained device exhibits a high electroluminescence (EL) above 20 000 cd m^{-2} and a stable EL spectrum with nearly unchanged Commission International de L'Eclairage (CIE) coordinate at a wide range of applied voltages. These results clearly demonstrate that the molecular encapsulation of the TADF blue host is a superior and promising strategy to achieve high performance and color stable solution-processed hybrid WOLEDs.

Introduction

White organic light-emitting diodes (WOLEDs) have received intensive interest due to their potential applications in solid-state lighting and flexible displays.[1] Generally, phosphorescent emitters are preferentially chosen to construct the devices since they can allow for a conversion of both singlet and triplet excitons into emitted photons and lead to a theoretical internal quantum efficiency of 100%.[2] However, due to the defect of blue phosphorescence, the device lifetime and color stability restrict the development of all-phosphorescent WOLEDs.[3] As an alternative, hybrid WOLEDs composed of a stable blue fluorescence and complementary phosphorescent emitters have been widely developed.[4] In order to simultaneously achieve a high efficiency and long device lifetime of hybrid WOLEDs, the prerequisite is the harvesting of triplet excitons on blue fluorescence without sacrificing the intrinsic blue emission.[5] The recent rise of thermally activated delayed fluorescence (TADF) with a small singlet–triplet energy gap (E_{ST}) can fulfill the requirements.[6] The electrogenerated triplet excitons of the blue host can upconvert to a singlet state through reversed intersystem crossing (RISC) and then transfer to the phosphorescent dopant by a long range Förster energy transfer (FET) process.[7] As a result, highly efficient hybrid WOLEDs with EQE above 20% and excellent stability have been reported based on a blue TADF emitting layer doped with an orange phosphorescent emitter.[8]

Although the strategy with a fluorescent material as a blue emitter and host for an orange phosphor has been successfully applied in vacuum-deposited hybrid WOLEDs, the device efficiency will severely decrease when transferring this concept to solution-processed hybrid WOLEDs.[9] Even using a TADF emitter as the blue host, the maximum EQE was only 10.1%, which is far behind the state-of-the-art vacuum-deposited hybrid WOLEDs.[10] Normally, the design concept featuring

[a]Jiangsu Key Laboratory of Function Control Technology for Advanced Materials, School of Chemical Engineering, Huaihai Institute of Technology, Lianyungang, Jiangsu, 222005, P. R. China. E-mail: banxx@hhit.edu.cn

[b]School of Chemistry and Chemical Engineering, Southeast University, Nanjing, Jiangsu, 211189, P. R. China. E-mail: jiangw@seu.edu.cn

† Electronic supplementary information (ESI) available: Synthetic route, TGA curves, XRD spectra, CV curves, time resolved PL traces and NMR spectra of the compounds; PL spectra of blue thin films and UV absorption of the phosphor; EL spectra and external quantum efficiencies *versus* current density plots of the blue devices; device lifetimes of the hybrid WOLEDs. See DOI: 10.1039/c8sc05456h

a TADF blue host and phosphorescent orange guest for solution-processed WOLEDs is confronted with several problems. Although the low dopant concentration has reduced the exciton quenching of the phosphorescent guest, the inherent concentration quenching of the tightly-packed TADF host may be another possible method of energy loss, which was usually ignored in previous studies.[11] In principle, to achieve a theoretical maximum internal quantum efficiency for TADF based hybrid WOLEDs, a key prerequisite is that all the electrically generated excitons in the TADF blue host must be effectively harvested for light emission.[12] Since the doping concentration of the orange phosphor has to be precisely controlled to be very low for ideal white emission, the electro-excited excitons are mainly formed on the blue host and then partly transfer to the guest through long range FET.[13] Unfortunately, most of the TADF emitters intrinsically suffer the concentration quenching effect in a pure film state.[14] If the accumulated excitons have already been quenched in the tightly-packed TADF host, the hybrid device would never get 100% internal quantum efficiency. Even worse, Aziz *et al.* recently demonstrated that the solution-processed emission layers are more sensitive to aggregation induced exciton quenching than the vacuum-evaporated ones due to the severe exciton–polaron interaction,[15] which explains why few of the small molecular TADF materials designed for vacuum-deposited devices can be successfully used as solution-processible hosts to achieve high performance OLEDs.

In this work, we designed and synthesized two TADF compounds, OCzBN and Cz-OCzBN, as solution-processible blue hosts for hybrid WOLEDs. Surprisingly, the device efficiencies based on Cz-OCzBN are much higher than those of OCzBN despite both the compounds having similar photophysical properties in the solution and film states. The experimental and theoretical analysis indicates that the encapsulated molecule Cz-OCzBN with unconjugated carbazoles as steric shields not only keeps the intrinsic TADF feature unchanged, but also restricts the triplet–triplet and triplet–polaron interaction induced exciton quenching. Moreover, the flexible alkyl chains enhance the solubility and film forming ability of the material, which makes Cz-OCzBN more efficient for the solution process. As a result, the optimized WOLED host with Cz-OCzBN shows the maximum current efficiency (CE) of 45.6 cd A^{-1}, power efficiency (PE) of 40.9 lm W^{-1}, and external quantum efficiency (EQE) of 17.0%, which are among the highest values reported for solution-processed hybrid WOLEDs. Furthermore, the maximum electroluminescence (EL) of the device is above 20 000 cd m^{-2} and the EL spectra are quite stable with a nearly unchanged CIE coordinate of (0.34, 0.44) at a wide range of applied voltages. In contrast, the device based on the unencapsulated parent emitter OCzBN only exhibits a maximum CE, PE and EQE of 14.8 cd A^{-1}, 10.4 lm W^{-1} and 5.5%, respectively. The more than tripled enhancement of the Cz-OCzBN based device fully demonstrates the importance of molecular encapsulation in facilitating the triplet utilization of the TADF blue host, which means the potential energy leakage pathway induced by intermolecular interaction can be efficiently resisted in the

tightly-packed film state. This research provides a useful strategy to qualify the small molecular TADF emitter as the blue host for constructing highly efficient solution-processed hybrid WOLEDs.

Results and discussion

The design route of the encapsulated TADF molecule is illustrated in Scheme 1. Both the emission core OCzBN and the encapsulated compound Cz-OCzBN are synthesized through one step catalyst free aromatic nucleophilic substitution reactions with the productive rate above 85% (Scheme S1†). The two materials are cost effective since no precious metals are required during the synthetic process. Both OCzBN and Cz-OCzBN are obtained as bright green powders, and their well-defined molecular structures were confirmed by ^{1}H-NMR, ^{13}C-NMR, mass spectrometry and elemental analysis.

The thermal properties of OCzBN and Cz-OCzBN were investigated using thermogravimetric analysis (TGA) and differential scanning calorimetry (DSC). As shown in Fig. S1,† the decomposition temperatures (T_d, with 5% weight loss) of OCzBN and Cz-OCzBN are 399 and 395 °C, respectively, which ensure good thermal stability during the heating and annealing of the solution process. On the other hand, the high glass transition temperatures (T_g) of OCzBN and Cz-OCzBN are 150 and 100 °C, respectively. The high T_g of the materials can facilitate the morphological stabilities and guarantee the long-term reliability of the devices. Comparing to the rigid structure of OCzBN, the introduced alkyl chains make Cz-OCzBN more flexible, which is the main reason for the reduced T_g of Cz-OCzBN.

In order to investigate the aggregation state, the scanning electron microscopy (SEM) spectra of the two compounds in the solid phase were obtained. As shown in Fig. 1c and d, Cz-OCzBN are amorphous particles in the solid state, while OCzBN exhibits a tightly aggregated polycrystalline state. X-ray diffraction (XRD) analyses of OCzBN and Cz-OCzBN were also performed. As shown in Fig. S2,† the sharp peaks in the diffraction pattern of OCzBN prove the existence of crystallization. In contrast, no peaks are found in the XRD spectrum of Cz-OCzBN, which indicates that the flexible chain linked carbazole units can remarkably decrease the crystallization tendency and suppress the aggregation between the molecules.
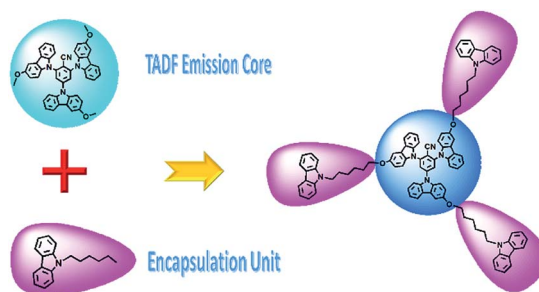
Scheme 1 Design route of the encapsulated TADF molecule and the molecular structures of OCzBN and Cz-OCzBN.
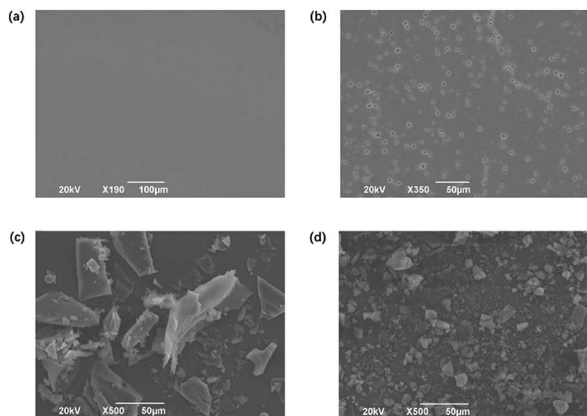
Fig. 1 The SEM images of (a) the vacuum-deposited OCzBN film, (b) the solution-processed OCzBN film, (c) OCzBN in the solid state, and (d) Cz-OCzBN in the solid state.

The thin films of OCzBN from both solution and vacuum processes were fabricated and characterized by SEM. As shown in Fig. 1a and b, the vacuum-deposited OCzBN shows a homogeneous film with no defect, whereas the solution-coated film exhibited pinholes over the entire film surface. The significant morphological difference between vacuum and solution-processed films indicates that the solution-coating procedure easily results in molecular aggregation and crystallization, which produces films with pinholes and cracks. Cz-OCzBN was designed to enhance the film forming ability by introducing alkyl-chain linked carbazoles as steric shields to enlarge the distance between OCzBN units and reduce the aggregation tendency.

To demonstrate the superiority of the encapsulated material in terms of film forming ability, the solution-processed thin films of OCzBN and Cz-OCzBN were analysed by atomic force microscopy (AFM). As shown in Fig. 2, although both materials can develop amorphous films by spin-coating, OCzBN shows many cracks and pinholes in the whole film, which can be assigned to the rigidity molecular structure and small
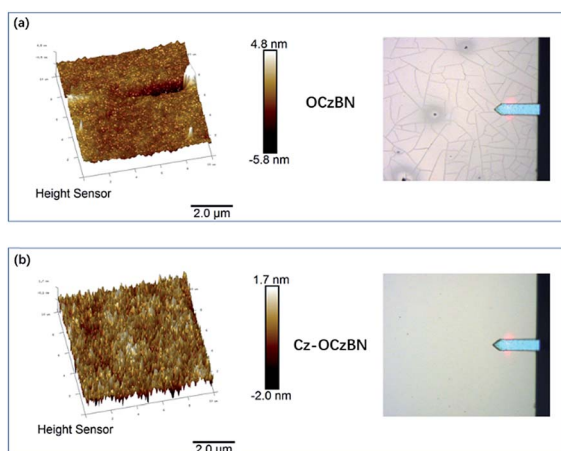
molecular weight. In contrast, Cz-OCzBN exhibits a homogeneous surface without any cracks or pinholes. The roughness of the partial area in a 10 μm × 10 μm square of Cz-OCzBN is measured to be 0.62 nm, while a clear groove was scanned in the same size small area of OCzBN. The enhanced film forming ability of Cz-OCzBN can be attributed to the introduced flexible chains and steric shields, which not only increase the molecular weight, but also improve the solubility and flexibility.

In order to get insight into the properties of the two TADF molecules, electronic cloud distributions and frontier orbital energy levels of OCzBN and Cz-OCzBN were calculated by density functional theory (DFT) calculations at the B3LYP/6-31G(d) level. As shown in Fig. 3, the optimized geometries of the two molecules exhibit a large dihedral angle between the phenyl core and carbazole units. The HOMO of OCzBN is primarily located on the electron-rich carbazole units and the LUMO resides on the electron-deficient benzonitrile group. Notably, in view of the unconjugated alkyl chain, no energy levels of Cz-OCzBN distribute on the peripheral units, which proves that the unconjugated carbazoles only act as shield moieties surrounding the electronically active emissive core in terms of steric effect. Thus, it is reasonable to draw the conclusion that the whole molecule of Cz-OCzBN can be divided into two independent functional fragments. The emissive core guarantees the electronic property of the molecule, while the peripheral carbazoles act as the steric shield of the emissive core to reduce the intermolecular interaction.

To further investigate the triplet spin-density distribution (SDD), DFT calculations for the lowest excited triplet states of OCzBN and Cz-OCzBN were also performed. As can be seen, the triplet spin-density of OCzBN distributes over the whole molecule, indicating the permanent triplet–triplet interaction in the tightly-packed pure film. Thus, the concentration quenching effect of OCzBN would be severe, just like most reported TADF molecules. In contrast, the triplet spin-density distribution of Cz-OCzBN was confined on the emissive core, which is surrounded by the flexible linked carbazole units. The steric effect substantially shields the triplet of the emissive core from contact with adjacent molecules due to the increased intermolecular distance. Since orbital overlaps are the prerequisite for efficient intermolecular electron interactions, it can be anticipated that the triplet–triplet and triplet–polaron quenching of

Fig. 2 AFM 3D height images (10 μm × 10 μm) and the corresponding topographic images of (a) OCzBN and (b) Cz-OCzBN.
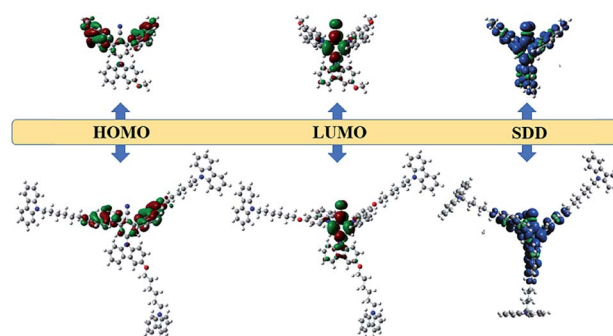

Fig. 3 Optimized geometries and calculated HOMO and LUMO density maps for OCzBN (up) and Cz-OCzBN (down).

Cz-OCzBN can be greatly suppressed by the introduction of unconjugated carbazoles as steric shields.

The theoretical calculated HOMO/LUMO energy levels of OCzBN and Cz-OCzBN are −5.23/−1.82 and −5.28/−1.83 eV (Table 1), while the S_1/T_1 energy levels are 2.79/2.68 eV and 2.82/2.69 eV, respectively. Thus, the calculated ΔE_{ST} of OCzBN and Cz-OCzBN are 0.11 and 0.13 eV, which would ensure efficient RISC and subsequently efficient TADF emission. The electrochemical properties of the materials were examined by cyclic voltammetry with ferrocene as the reference and both compounds exhibit multiple irreversible oxidation curves (Fig. S3†). The HOMO levels were derived using the following equation: $HOMO = -(E_{ox} - E_{Fc/Fc^+}) - 4.8$ eV. According to the onset of the oxidation peak, the HOMO energy levels of OCzBN and Cz-OCzBN are estimated to be both −5.49 eV. Based on the optical energy band gaps, the LUMO energy levels of OCzBN and Cz-OCzBN are calculated to be −2.46 and −2.49 eV, respectively. The similar HOMO and LUMO levels of OCzBN and Cz-OCzBN can be ascribed to the identical distribution of their frontier molecular orbitals.

Fig. 4 shows the ultra-violet (UV), photoluminescence (PL) and phosphorescence (PH) spectra of the two materials. The absorption spectrum of Cz-OCzBN exhibits similar patterns to that of its parent core OCzBN. The long wavelength absorptions beyond 350 nm are assigned to the charge transfer states from the carbazole to benzonitrile units, while the increased absorption intensity at 250–300 nm can be attributed to the introduced peripheral carbazole side chains. According to the edges of the absorption spectra, the energy gaps (E_g) of OCzBN and Cz-OCzBN are 3.03 and 3.00 eV. The PL emission wavelengths of OCzBN and Cz-OCzBN in toluene are 456 and 459 nm, respectively, under UV excitation at a wavelength of 330 nm. The similar PL spectra indicate that the encapsulated material Cz-OCzBN gets the PL emission from its parent emissive core. Based on the onset of the broad emission bands, the singlet energies of OCzBN and Cz-OCzBN are 3.02 and 2.99 eV, respectively, while the triplet energies, determined by the highest-energy vibronic sub-band of the phosphorescence spectra at 77 K, are both 2.82 eV. Therefore, the experimental ΔE_{ST} of OCzBN and Cz-OCzBN are calculated to be 0.20 eV and 0.17 eV, respectively. To reveal the characteristics of the TADF process, the transient behaviors of the films are measured. Fig. 5a shows the PL decay curves of OCzBN and Cz-OCzBN excited by a 280 nm laser and detected at 480 nm. Both compounds clearly exhibit the prompt and delayed parts in the transient decay curves. In the range of nanoseconds, OCzBN and Cz-OCzBN show prompt decays with lifetimes of 26 and 32
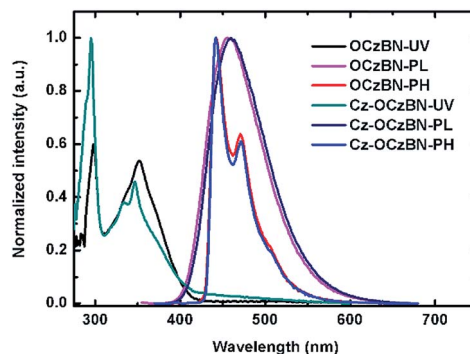

Fig. 4 The UV, PL and PH spectra of OCzBN and Cz-OCzBN in toluene.

ns, respectively, which could be attributed to the direct fluorescence process from singlet states (S_1) to ground states (S_0). While in the order of microseconds, the lifetimes of the delay components are measured to be 1.3 μs for OCzBN and 1.5 μs for Cz-OCzBN, respectively, which should be ascribed to the TADF process. The improved delayed lifetime of Cz-OCzBN indicates that molecular encapsulation can facilitate the triplet utilizations for delay emission due to the reduction of intermolecular interaction induced triplet–triplet exciton quenching. Comparing to Cz-OCzBN, the delayed component in the OCzBN neat film was relatively weaker due to the deactivation of the accumulated excitons induced by intermolecular interaction in the intensive aggregated state. This result illustrates the key role of encapsulation in facilitating the utilization of triplet excitons in pure film states.

To further demonstrate the TADF property of OCzBN and Cz-OCzBN, the time-resolved photoluminescence spectra in the film state were also measured. As shown in Fig. S4,† the similar photoluminescence spectra were obtained before and after applying the delay time, which confirms that the delayed emission comes from the singlet states by a reversed process. Normally, TADF materials undergo severe concentration quenching in pure film states. When using TADF materials as a host, the exciton quenching in the TADF host will inevitably reduce the device efficiency. In order to eliminate the quenching effect of the traditional TADF emitter, the newly designed blue TADF material with alkyl chain linked carbazoles as steric shields was developed to suppress the intermolecular interaction. The photoluminescence quantum yield (PLQY) of OCzBN and Cz-OCzBN in neat films have been measured. The PLQY of OCzBN and Cz-OCzBN are 42% and 58%, respectively. The

Table 1 Physical properties of OCzBN and Cz-OCzBN

	T_d/T_g [°C]	λ_{abs} [nm][a]	λ_{ems} [nm]	E_g [eV]	S_1/T_1 [eV]	ΔE_{ST} [eV]	HOMO [eV]	LUMO [eV]
OCzBN	399/150	297, 335, 352, 370	456[a], 483[b]	3.41[c], 3.03[d]	2.79/2.68[c], 3.02/2.82[e]	0.11[c], 0.20[e]	−5.23[c], −5.49[f]	−1.82[c], −2.46[g]
Cz-OCzBN	395/100	294, 328, 340, 370	459[a], 478[b]	3.45[c], 3.00[d]	2.82/2.69[c], 2.99/2.82[e]	0.13[c], 0.17[e]	−5.28[c], −5.49[f]	−1.83[c], −2.49[g]

[a] Measured in toluene solution at 300 K. [b] Measured in deposited films at 300 K. [c] Obtained from Gauss simulation. [d] Estimated from the absorption edges in CH_2Cl_2. [e] Estimated from fluorescence and phosphorescence spectra. [f] Determined by the CV measurement. [g] Calculated from the energy gap and HOMO level.
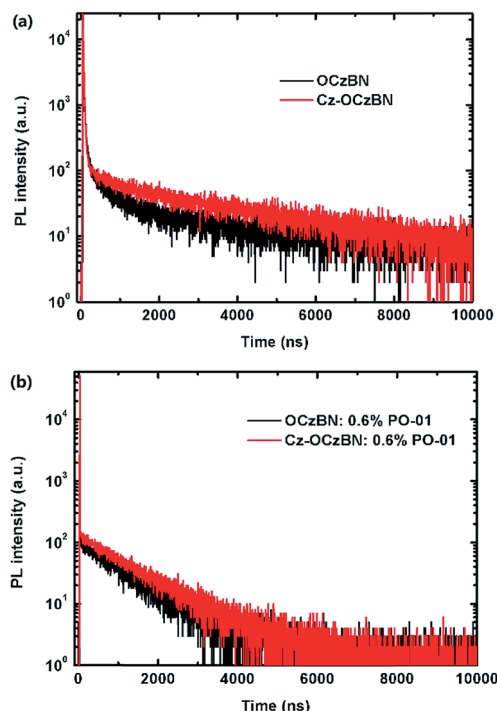
Fig. 5 (a) The transient PL decay curves of OCzBN and Cz-OCzBN films detected at 480 nm. (b) The transient PL decay curves of OCzBN:0.6% PO-01 and Cz-OCzBN:0.6% PO-01 films detected at 560 nm.

enhanced PLQY of Cz-OCzBN demonstrate the hypothesis that molecular encapsulation can reduce exciton quenching in the films. Moreover, the similar UV-vis absorptions, PL spectra and time resolved PL traces indicate that the molecular encapsulation by unconjugated flexible linked carbazole keeps the PL characteristic and TADF property unchanged.

Since the triplet energy of OCzBN and Cz-OCzBN (2.82 eV) is much higher than that of the orange phosphor PO-01 (2.2 eV), both TADF emitters can be used as a blue host for PO-01 without back energy leakage. Moreover, the spectral overlap between the absorption of PO-01 and the PL of OCzBN or Cz-OCzBN implies that efficient Förster energy transfer can be anticipated (Fig. S5†). To confirm the presence of energy transfer, the PL transient decay characteristic of blue TADF:0.6 wt% PO-01 doped films are investigated. Fig. 5b shows the transient PL decay curves of blue TADF:0.6 wt% PO-01 at the emission of 480 nm, which corresponds to the TADF host emission. The lifetime of the prompt parts and the ratio of the delayed parts of OCzBN and Cz-OCzBN are reduced after adding dopant PO-01, which indicates energy transfer from TADF host to dopant. Since only singlet excitons are directly formed in the TADF hosts under PL excitation, the lifetimes of the prompt part of the hosts (τ_S) and the energy transfer efficiency (η_{ET}) from host to guest can be expressed as:

$$\eta_{ET} = 1 - \frac{\tau_S}{\tau_{S_0}} \tag{1}$$

$$\tau_S = \frac{1}{k_r + k_{nr} + k_{ISC} + k_{ET}} \tag{2}$$

where, k_r is the radiative transition, k_{nr} is the nonradiative transition, k_{ISC} is the intersystem crossing rate, and k_{ET} is the energy transfer rate. According to the data list in Table S1,† the k_{ET} of OCzBN and Cz-OCzBN are 3.29×10^7 and 5.96×10^7, while the η_{ET} of OCzBN and Cz-OCzBN are 45% and 62%, respectively. The improved energy transfer efficiency of Cz-OCzBN indicates that Cz-OCzBN possesses more efficient energy transfer from its singlet state to the phosphorescent dopant than OCzBN with the same dopant concentration. Moreover, the transient PL decay curves of the emission at 560 nm, which correspond to the PO-01 emission, were also detected. Under PL excitation, only singlet excitons are directly formed on the hosts, the triplet excitons of the hosts can only be formed through the ISC process. The long lifetime of PO-01 at a low dopant concentration can be attributed to the energy transfer from the delayed singlet excitons of the host, which were upconverted from the triplet states. As shown in Fig. S6,† the increased delay part of Cz-OCzBN:0.6%PO-01 compared to OCzBN:0.6%PO-01 also demonstrates that Cz-OCzBN can harvest more triplet excitons for energy transfer. Fig. 6 shows the PL spectra of OCzBN:PO-01 and Cz-OCzBN:PO-01 at different doping concentrations. As can be seen, the PL emission of OCzBN and Cz-OCzBN were gradually decreased with the increasing PO-01 doping concentration, which indicates that the energy transfer from the blue host to the orange dopant was efficient and appropriate white emission can be expected by finely adjusting the concentration of PO-01.

To investigate the fundamental electroluminescence property of the two TADF emitters, solution-processed non-doped OLEDs based on the neat films were fabricated with the
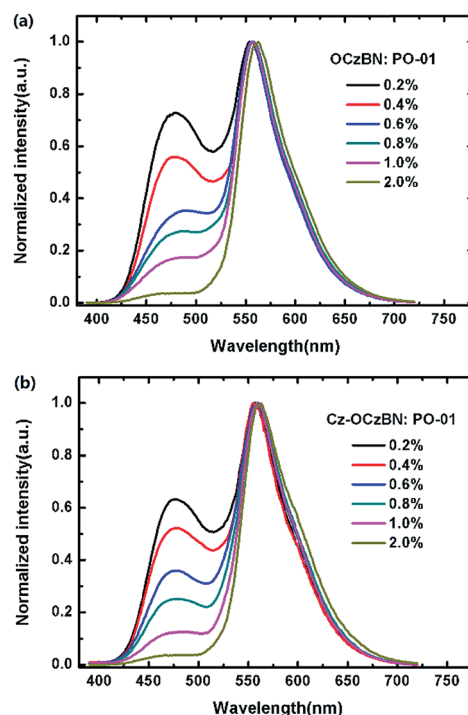

Fig. 6 The emission spectra of the PO-01 doped films of (a) OCzBN and (b) Cz-OCzBN.

structure of ITO/PEDOT:PSS (40 nm)/EML (60 nm)/TPBI (40 nm)/Cs_2CO_3 (2 nm)/Al. The current density–voltage–luminance curves and external quantum efficiency–current density characteristics are shown in Fig. S7.† As shown in Fig. S8,† Cz-OCzBN exhibits an EL spectrum identical to its PL emission with Commission Internationale de L'Eclairage (CIE) coordinates of (0.18, 0.29), while the EL spectrum of OCzBN was red shifted with a CIE of (0.22, 0.41). Even worse, a low energy emission around 600 nm was founded with an increased driving voltage (Fig. 7), which indicates the formation of severe aggregated state under electro-excitation. In contrast, Cz-OCzBN shows a high color purity with the EL spectra independent of the applied voltages from 8 to 12 V, which means the intermolecular interaction induced aggregation was inhibited by efficient molecular encapsulation. As a result, the maximum EQE of Cz-OCzBN is 6.6%, which is higher than that of conventional fluorescent OLEDs (<5%). The improved EQE indicates that Cz-OCzBN can intrinsically harvest triplet excitons for light emission through a TADF process. Although OCzBN is also a TADF material, the maximum EQE of its pure film was only 1.5%, which was much lower than that of encapsulated Cz-OCzBN. The poor EL efficiency of the OCzBN based non-doped device can be attributed to the inevitable triplet–triplet or triplet–polaron interaction induced exciton quenching in the tightly packed film. These results fully demonstrate that molecular encapsulation by introducing carbazole units as steric shields can effectively restrict the concentration quenching in a TADF emitter and facilitate triplet exciton utilization.

Based on the above device structure, single emission layer hybrid WOLEDs were fabricated by doping orange phosphor PO-01 into blue emitter OCzBN and Cz-OCzIPN. The dopant concentration of PO-01 was optimized to be 0.6 wt% to ensure the spectral quality. Fig. 8 shows the proposed energy level diagram of the fabricated hybrid WOLEDs and the chemical structures of the materials used. Fig. 9a and b show the EL spectra of the WOLEDs at different voltages. Both the devices exhibit white emissions with blue peaks at around 480 nm and orange peaks around 562 nm, which are in accordance with the emission of the blue TADF emitter and orange phosphor. The CIE coordinates are (0.35, 0.46) and (0.34, 0.44) for OCzBN and Cz-OCzIPN based devices, respectively. Moreover, the emission spectra are quite stable with an extremely small CIE variation in the wide range of voltages from 8 to 12 V. Usually, the color stabilities of single-EML WOLEDs are poor with the blue emission intensity enhanced under high current density due to the inefficient triplet energy transfer from the blue host to the orange dopant.[13a,d,17] Unlike the traditional fluorescence host, the TADF blue host can facilitate triplet utilization by efficient up-conversion, which ensures the color stability of single emission layer white devices.[8b,12c,13b]

Fig. 9c and d show the current density–voltage–luminance (J–V–L) characteristics and the device efficiency versus current density plots. Both the devices have low turn-on voltages of 3.4 V (Table 2), indicating that the suitable HOMO and LUMO levels could facilitate charge injections in the devices. The optimized solution-processed hybrid WOLED based on Cz-OCzBN shows an excellent EL performance with maximum CE, PE and EQE of 45.6 cd A^{-1}, 40.9 lm W^{-1} and 17.0%, respectively, which are among the highest values of reported solution-processed hybrid WOLEDs (Table 3). Moreover, the EQE still remains as high as 15.3% and 12.0% at the brightness of 100 and 1000 cd m^{-2}, showing small efficiency roll-off compared to other solution-processed WOLEDs. In contrast, the OCzBN based hybrid WOLED only exhibits a maximum CE, PE and EQE of 14.8 cd A^{-1}, 10.4 lm W^{-1} and 5.5%, respectively. Even worse, the luminescence of the OCzBN based device undergoes severe luminescence roll-off at a high current density, which indicates the existence of some remaining exciton quenching in such a device.

To study the stability of the devices, the operation lifetime of the two white OLEDs was measured. Fig. S9† shows the normalized luminance of the devices as a function of
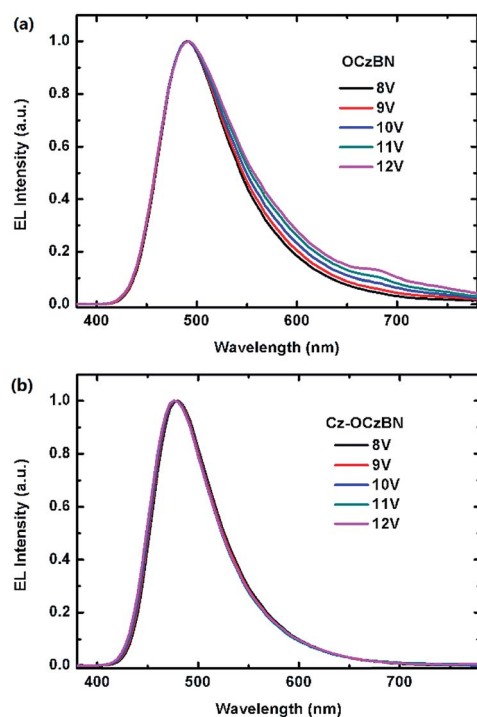

Fig. 7 The EL spectra of the blue devices at different voltages of (a) OCzBN and (b) Cz-OCzBN.
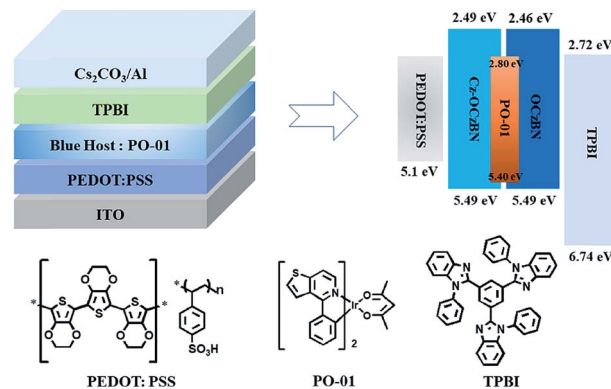

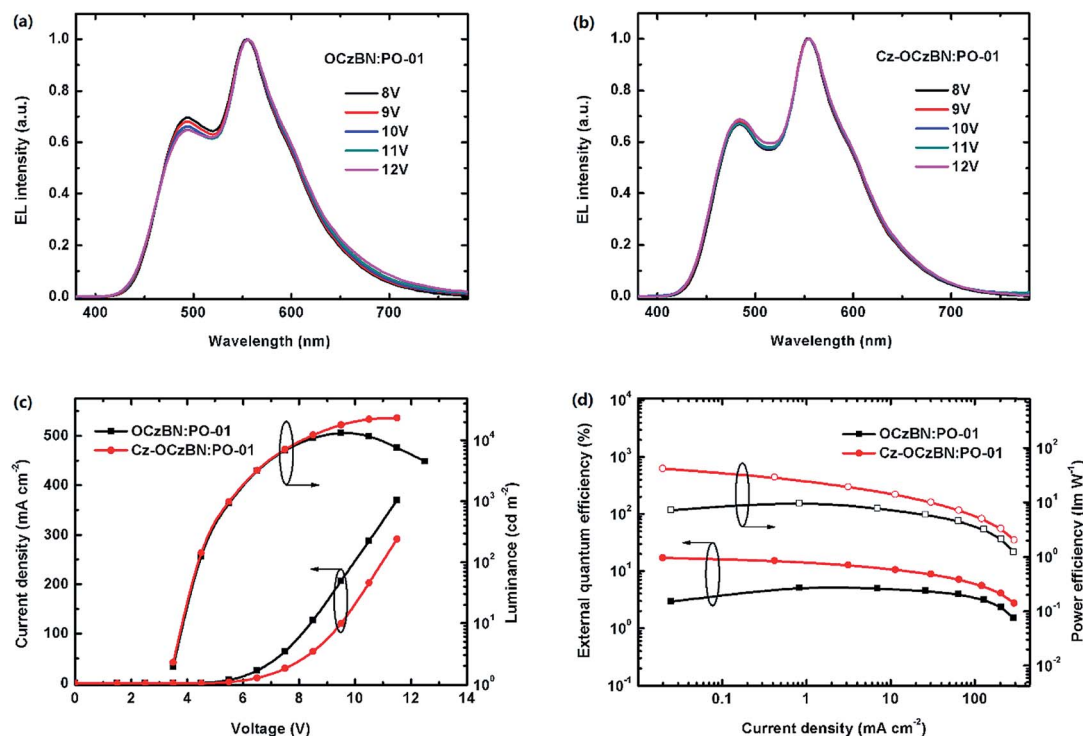Fig. 8 The energy diagram of the devices and the molecule structures.

Fig. 9 The EL spectra of the hybrid WOLEDs at different voltages of (a) OCzBN:PO-01 and (b) Cz-OCzBN:PO-01; (c) current density−voltage−luminance (J−V−L) characteristics; (d) external quantum efficiency and power efficiency *versus* current density plots.

operational time at an initial luminance L_0 of 1000 cd m^{-2}. The LT50 (defined as the operating lifetime at 50% of the initial luminance) of the OCzBN-based device is only 1.25 h, while the Cz-OCzBN-based white device exhibited a much longer lifetime with an LT50 of 24.5 h. The enhanced operating lifetime indicates that the molecular encapsulation promotes device stability. Since the device structure and the phosphor dopant of the two WOLEDs are the same, the different device performance both in device efficiency and device stability indicates the different exciton harvesting abilities of OCzBN and Cz-OCzBN.

Fig. 10 shows the working mechanism of TADF based hybrid WOLEDs. In order to achieve ideal white emission, the dopant concentrations of the orange phosphors in the single-EML hybrid WOLEDs are usually controlled below 1 wt%. Thus, the energy transfer from the host triplet to the phosphor dopant through the Dexter transfer mechanism, which is a short-range interaction, can be ignored due to the extremely low dopant concentration. Thanks to the TADF

property, the triplet excitons of the blue host can be thermally upconverted into their singlet and then transferred to the phosphor dopant through Förster energy transfer. Therefore, hybrid WOLEDs using a TADF blue host can theoretically harvest all the electrogenerated excitons for radiative transition. However, the majority of triplet excitons will reside in the blue host before they can be efficiently transferred to the orange phosphor. The accumulated triplet excitons in the tightly-packed blue host will inevitably promote the severe triplet–triplet and triplet–polaron quenching, which are the dominating energy leakage pathways in such a device structure. Moreover, the above investigations demonstrate that the particular make-up of the solution-processed EML makes OCzBN more sensitive to the intramolecular interaction induced exciton quenching, which may be the main reason why few small molecular TADF materials have been successfully developed as solution-processible blue hosts for hybrid WOLEDs.[15] As a result, even though OCzBN possesses efficient

Table 2 Device performances of the solution-processed hybrid WOLEDs

Device	V_{on}^a [V]	CE_{max}^b [cd A^{-1}]	PE_{max}^c [lm W^{-1}]	EQE_{max}^d [%]	EQE_{100}^e [%]	EQE_{1000}^f [%]	L_{max}^g [cd m^{-2}]	CIE $[x, y]^h$
OCzBN:PO-01	3.4	14.8	10.4	5.5	5.3	4.4	13 100	(0.35, 0.46)
Cz-OCzBN:PO-01	3.4	45.6	40.9	17.0	15.3	12.0	23 400	(0.34, 0.44)

^{a} V_{on} = turn-on voltage at 1 cd m^{-2}. ^{b} CE_{max} = maximum current efficiency. ^{c} PE_{max} = maximum power efficiency. ^{d} EQE_{max} = maximum external quantum efficiency. ^{e} EQE at 100 cd m^{-2}. ^{f} EQE at 1000 cd m^{-2}. ^{g} L_{max} = maximum luminance. ^{h} CIE = the Commission Internationale de L'Eclairage coordinates at the luminance of 1000 cd m^{-2}.

Table 3 Summary of EL performance of solution-processed hybrid WOLEDs

| Solution-processed EML	EQE$_{max}$ [%]	PE$_{max}$ [lm W^{-1}]	CE$_{max}$ [cd A^{-1}]	CIE [x, y]	
Blue TADF:orange phosphor	17.0	40.4	45.6	(0.34, 0.44)	This work
Blue TADF:orange phosphor	10.1	—	17.7	(0.32, 0.33)	Ref. 10
Host: blue TADF:red phosphor	6.16	—	11.58	(0.32, 0.33)	Ref. 9b
Host: blue TADF:orange phosphor	6.59	—	17.34	(0.41, 0.41)	Ref. 11b
Host: blue TADF:orange phosphor	12.4	17.2	29.1	(0.36, 0.41)	Ref. 9a
Host: blue TADF:orange phosphor	12.3	18.1	28.8	(0.36, 0.43)	Ref. 18
Blue AIE:orange phosphor	—	1.8	3.4	(0.36, 0.43)	Ref. 11a
Blue polymer:red phosphor	3.11	1.36	2.77	(0.36, 0.44)	Ref. 19
Blue polymer:yellow phosphor	2.8	—	4.57	(0.34, 0.36)	Ref. 9f
Blue polymer:green/red phosphor	—	5.5	9.0	(0.33, 0.33)	Ref. 9e
Blue polymer:blue/yellow/red phosphor	12.6	15.2	21.4	(0.35, 0.33)	Ref. 9c
Blue dendrimer:green/red phosphor	8.5	7.7	16.9	(0.31, 0.33)	Ref. 9d
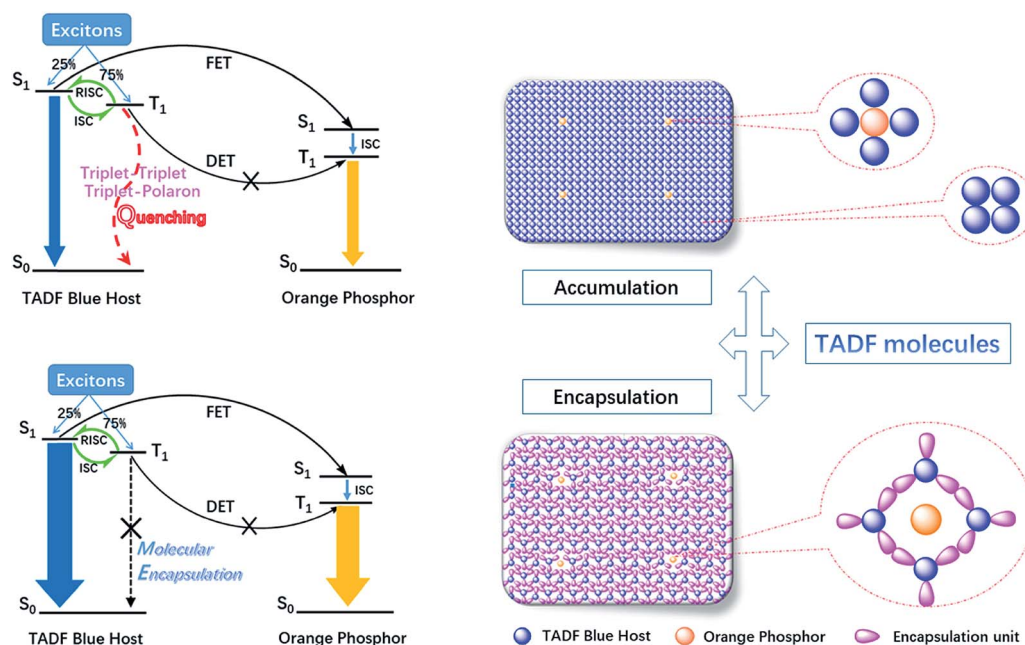
Fig. 10 The energy transfer diagram from the TADF blue host emitter to the orange phosphor and the morphology diagram of the aggregates in the film state.

TADF properties, the solution-processed hybrid WOLEDs based on it can only achieve a poor device performance.

It has been reported that triplet–triplet annihilation (TTA) and triplet–polaron quenching (TPQ) are the main reasons for the reduction of device efficiency and stability. However, the encapsulated molecule Cz-OCzBN with peripheral carbazole units, which act as steric shields to reduce the intermolecular interactions between the emissive cores in the tightly-packed film state, will efficiently suppress the short-range interaction induced TTA and TPQ. Therefore, more triplet excitons of Cz-OCzBN can upconvert to singlet excitons, either decay through blue emission or be transferred to the orange phosphor dopant, and will facilitate triplet utilization under a high current density, which is helpful to enhance the device efficiency and reduce the efficiency roll-off. As a result, the observed performance of solution-processed hybrid WOLEDs

based on Cz-OCzBN was dramatically improved by almost three times for device efficiency and twenty times for device lifetime compared to the OCzBN based one. These findings clearly demonstrate that the present encapsulated TADF emitter is a potential candidate as a blue host for solution-processed hybrid WOLEDs.

Conclusions

In conclusion, two TADF emitters, OCzBN and Cz-OCzBN, were designed and synthesized as blue hosts for solution-processed hybrid WOLEDs with a single-EML. In particular, the experimental and theoretical analysis shows that the encapsulated molecule Cz-OCzBN with peripheral carbazoles linked by flexible alkyl chains is more efficient for solution-processed devices due to the enhanced film forming ability and triplet exciton

utilization. The resulting solution-processed hybrid WOLEDs achieved excellent performance with superior CE, PE and EQE of 45.6 cd A^{-1}, 40.9 lm W^{-1} and 17.0%, respectively, which are among the highest values of the reported solution-processed hybrid WOLEDs. In addition, the device shows a stable EL spectrum with nearly unchanged CIE coordinates of (0.34, 0.44) at a wide range of applied voltages. The present study reports a simple approach to significantly boost the performance of solution-processed single-EML hybrid WOLEDs by molecular encapsulation of a TADF blue host, which can efficiently suppress the triplet–triplet and triplet–polaron quenching of the excitons during electro-excitation. It can be anticipated that this strategy might stimulate further research of efficient TADF blue hosts for high-performance solution-processed hybrid WOLEDs.

Experimental section

General methods

All the reagents used for the synthesis of the compounds were purchased from Aldrich and Acros companies and used without further purification. The anhydrous tetrahydrofuran (THF) solvent was dewatered according to standard procedures. The intermediates 3-methoxy-9H-carbazole (OCz) and 9-(6-(9H-carbazol-3-yloxy)hexyl)-9H-carbazole (Cz-OCz) were prepared according to the literature procedure.[16] ^{1}H and ^{13}C NMR spectra were recorded on a BRUKER AMX instrument. Elemental analysis was performed using an Elementar Vario EL CHN elemental analyzer. Molecular masses were measured by a BRUKER DALTONICS matrix-assisted laser desorption-ionization time-of-flight mass spectrometer (MALDI-TOF-MS). The UV-vis absorption spectra of the compounds were measured by SHIMADZU UV-2450. The photoluminescence emission spectra were recorded on HORIBA FLUOROMAX-4. Thermogravimetric analysis (TGA) and differential scanning calorimetry (DSC) curves were recorded with a Netzsch simultaneous thermal analyzer (STA) system (STA 409PC) and DSC 2910 modulated calorimeter under a dry nitrogen gas flow at a heating rate of 10 °C min^{-1}. Cyclic voltammetry (CV) was performed on a CHI750C voltammetric analyzer in a typical three-electrode cell with a platinum plate working electrode, a platinum wire counter electrode and a silver wire reference electrode. The optimized structure was calculated by Gaussian09 at the B3LYP functional with 6-31G (d) basis sets. The excitation energies in the singlet and triplet states were obtained using the TD-DFT method based on an optimized molecular structure for the ground state. The scanning electron microscopy (SEM) images were obtained from a JSM-6390LA. The elemental mapping of the produced films was performed using an energy dispersive X-ray (EDX) microanalyzer (EMAX300, Horiba).

Device fabrication and measurements

ITO-coated glass substrates were rinsed in deionized water and then ultrasonicated sequentially in acetone and ethanol. Before device fabrication, the ITO substrate was treated in a UV–ozone

oven for 20 min. Then 40 nm PEDOT:PSS was spin-coated onto the ITO substrate and dried at 200 °C for 10 min. The substrates were then taken into a nitrogen glove box, where the 60 nm emission layer was spin coated onto the PEDOT:PSS layer from chlorobenzene and annealed at 100 °C for 30 min. After that, 40 nm TPBI was vacuum-deposited as the electron transporting layer. Finally, Cs$_2$CO$_3$ (2 nm) and Al (100 nm) were deposited as the cathode for the three devices. The EL spectra, device luminance, and current density–voltage characteristics were recorded using a combination of a Photo-Research PR-655 SpectraScan and a Keithley 2400 Sourcemeter. The device was tested in the condition of the atmosphere with no protective encapsulation.

Materials synthesis

Synthesis of 2,4,6-tris(3-methoxy-9H-carbazol-9-yl) benzonitrile (OCzBN). In the nitrogen atmosphere, the prepared OCz (0.68 g, 3.5 mmol) was added to the anhydrous THF solution (40 mL) containing NaH (0.60 g, 5 mmol). The mixture was stirred at 0 °C for 0.5 h, then 2,4,6-trifluorobenzonitrile (0.15 g, 1 mmol) in anhydrous THF (20 mL) was added dropwise. The solution was stirred for another 12 h at room temperature. After the reaction was over, the reaction was quenched with the addition of 250 mL water. The mixture was extracted with CH$_2$Cl$_2$ three times. The combined organic layer was dried with anhydrous MgSO$_4$ and the solvent was removed under vacuum. The precipitate was purified by column chromatography on silica gel, resulting in a bright green product (0.60 g, 88%). ^{1}H-NMR (500 MHz, CDCl$_3$, δ): 8.13 (d, J = 7.8 Hz, 2H), 8.06 (d, J = 7.7 Hz, 1H), 7.98 (s, 2H), 7.63 (dd, J = 5.3, 2.9 Hz, 3H), 7.54 (ddd, J = 17.5, 7.7, 5.1 Hz, 6H), 7.47–7.41 (m, 3H), 7.38–7.29 (m, 3H), 7.20–7.15 (m, 2H), 7.05 (dd, J = 8.9, 2.5 Hz, 1H), 3.97 (s, 6H), 3.92 (s, 3H). ^{13}C-NMR (101 MHz, CDCl$_3$, δ): 155.49, 155.28, 144.55, 141.00, 139.74, 135.33, 133.99, 126.80, 126.62, 125.35, 125.01, 125.00, 124.72, 124.50, 124.33, 121.57, 121.12, 120.82, 120.76, 115.38, 115.30, 113.32, 110.58, 110.56, 110.52, 109.91, 109.90, 109.73, 109.72, 109.20, 103.87, 103.78, 56.12, 56.04. HRMS (ESI) m/z: [M + H]$^{+}$ calcd for C$_{46}$H$_{32}$N$_4$O$_3$, 688.2474; found, 688.2463. Anal. calcd. for C$_{64}$H$_{32}$N$_4$O$_3$: C, 80.21; H, 4.68; N, 8.13. Found: C, 80.18; H, 4.70; N, 8.10.

Synthesis of (2R,6S)-2,4,6-tris(3-(6-(9H-carbazol-9-yl)hexyloxy)-9H-carbazol-9-yl)benzo-nitrile (Cz-OCzBN). This compound was prepared from intermediates Cz-OCz and 2,4,6-trifluorobenzonitrile following the same procedure as OCzBN. Bright green solid, yield: 86%. ^{1}H-NMR (500 MHz, CDCl$_3$, δ): 8.09 (dd, J = 15.2, 7.4 Hz, 8H), 8.03 (d, J = 7.8 Hz, 1H), 7.96 (s, 2H), 7.62 (d, J = 8.3 Hz, 1H), 7.59 (d, J = 2.3 Hz, 2H), 7.56–7.48 (m, 6H), 7.48–7.37 (m, 15H), 7.35 (t, J = 7.1 Hz, 2H), 7.30 (t, J = 7.5 Hz, 1H), 7.21 (q, J = 7.2 Hz, 6H), 7.13 (dd, J = 8.9, 2.4 Hz, 2H), 6.99 (dd, J = 9.0, 2.3 Hz, 1H), 4.38–4.28 (m, 6H), 4.07 (t, J = 6.3 Hz, 4H), 4.01 (t, J = 6.3 Hz, 2H), 1.99–1.87 (m, 6H), 1.87–1.75 (m, 6H), 1.63–1.52 (m, 6H), 1.51–1.42 (m, 6H). ^{13}C-NMR (101 MHz, CDCl$_3$, δ): 155.89, 155.84, 144.42, 144.20, 141.87, 140.68, 140.41, 139.69, 127.52, 127.39, 125.82, 124.01, 123.74, 123.39, 122.84, 121.54, 120.34, 118.74, 113.71, 113.59, 113.06, 110.41,

109.06, 108.96, 108.65, 108.59, 103.50, 103.20, 102.33, 102.12, 67.64, 42.97, 42.87, 29.01, 28.83, 27.17, 27.11, 27.02, 26.16, 26.06. HRMS (ESI) m/z: $[M + H]^+$ calcd for $C_{97}H_{83}N_7O_3$, 1393.6557; found, 1393.5981. Anal. calcd. for $C_{97}H_{83}N_7O_3$: C, 83.53; H, 6.00; N, 7.03. Found: C, 83.52; H, 6.04; N, 7.01.

Conflicts of interest

There are no conflicts to declare.

Acknowledgements

Notes and references

1 (a) T. Higuchi, H. Nakanotani and C. Adachi, *Adv. Mater.*, 2015, **27**, 2019; (b) T. Fleetham, Y. Ji, L. Huang, T. S. Fleetham and J. Li, *Chem. Sci.*, 2017, **8**, 7983; (c) C. Groves, *Nat. Mater.*, 2013, **12**, 597.

2 (a) G. Sarada, W. Cho, A. Maheshwaran, V. G. Sree, H.-Y. Park, Y.-S. Gal, M. Song and S.-H. Jin, *Adv. Funct. Mater.*, 2017, **27**, 1701002; (b) C.-C. Lai, M.-J. Huang, H.-H. Chou, C.-Y. Liao, P. Rajamalli and C.-H. Cheng, *Adv. Funct. Mater.*, 2015, **25**, 5548.

3 (a) B. Liu, H. Nie, X. Zhou, S. Hu, D. Luo, D. Gao, J. Zou, M. Xu, L. Wang, Z. Zhao, A. Qin, J. Peng, H. Ning, Y. Cao and B. Z. Tang, *Adv. Funct. Mater.*, 2016, **26**, 776; (b) C. J. Zheng, J. Wang, J. Ye, M. F. Lo, X. K. Liu, M. K. Fung, X. H. Zhang and C. S. Lee, *Adv. Mater.*, 2013, **25**, 2205; (c) B. Liu, X.-L. Li, H. Tao, J. Zou, M. Xu, L. Wang, J. Peng and Y. Cao, *J. Mater. Chem. C*, 2017, **5**, 7668.

4 (a) D. Luo, X.-L. Li, Y. Zhao, Y. Gao and B. Liu, *ACS Photonics*, 2017, **4**, 1566; (b) X. Ouyang, X.-L. Li, L. Ai, D. Mi, Z. Ge and S.-J. Su, *ACS Appl. Mater. Interfaces*, 2015, **7**, 7869; (c) X. K. Liu, Z. Chen, J. Qing, W. J. Zhang, B. Wu, H. L. Tam, F. Zhu, X. H. Zhang and C. S. Lee, *Adv. Mater.*, 2015, **27**, 7079; (d) F. Zhao, Y. Wei, H. Xu, D. Chen, T. Ahamad, S. Alshehri, Q. Pei and D. Ma, *Mater. Horiz.*, 2017, **4**, 641.

5 (a) J.-H. Jou, C.-Y. Hsieh, J.-R. Tseng, S.-H. Peng, Y.-C. Jou, J. H. Hong, S.-M. Shen, M.-C. Tang, P.-C. Chen and C.-H. Lin, *Adv. Funct. Mater.*, 2013, **23**, 2750; (b) Y. Liu, F. Liang, L.-S. Cui, X.-B. Shi, Z.-K. Wang and L.-S. Liao, *Adv. Opt. Mater.*, 2016, **4**, 2051; (c) B. Liu, D. Luo, J. Zou, D. Gao, H. Ning, L. Wang, J. Peng and Y. Cao, *J. Mater. Chem. C*, 2015, **3**, 6359; (d) X. Du, G. Li, J. Zhao, S. Tao, C. Zheng, H. Lin, Q. Tong and X. Zhang, *Adv. Opt. Mater.*, 2017, **5**, 1700498.

6 D. Zhang, L. Duan, Y. Zhang, M. Cai, D. Zhang and Y. Qiu, *Light:Sci. Appl.*, 2015, **4**, e232.

7 Z. Wu, L. Yu, F. Zhao, X. Qiao, J. Chen, F. Ni, C. Yang, T. Ahamad, S. M. Alshehri and D. Ma, *Adv. Opt. Mater.*, 2017, **5**, 1700415.

8 (a) S.-F. Wu, S.-H. Li, Y.-K. Wang, C.-C. Huang, Q. Sun, J.-J. Liang, L.-S. Liao and M.-K. Fung, *Adv. Funct. Mater.*, 2017, **27**, 1701314; (b) Z. Wu, J. Luo, N. Sun, L. Zhu, H. Sun, L. Yu, D. Yang, X. Qiao, J. Chen, C. Yang and D. Ma, *Adv. Funct. Mater.*, 2016, **26**, 3306.

9 (a) W. Li, J. Zhao, L. Li, X. Du, C. Fan, C. Zheng and S. Tao, *Org. Electron.*, 2018, **58**, 276; (b) C. W. Joo, H. Cho, B.-H. Kwon, N. S. Cho, Y. Kim, Y.-H. Kim and J. Lee, *J. Ind. Eng. Chem.*, 2018, **65**, 35–39; (c) S. Hu, M. Zhu, Q. Zou, H. Wu, C. Yang, W.-Y. Wong, W. Yang, J. Peng and Y. Cao, *Appl. Phys. Lett.*, 2012, **100**, 063304; (d) L. Wang, Y. Jiang, J. Luo, Y. Zhou, J. Zhou, J. Wang, J. Pei and Y. Cao, *Adv. Mater.*, 2009, **21**, 4854; (e) Y. Xu, J. Peng, J. Jiang, W. Xu, W. Yang and Y. Cao, *Appl. Phys. Lett.*, 2005, **87**, 193502; (f) H. A. Al Attar, A. P. Monkman, M. Tavasli, S. Bettington and M. R. Bryce, *Appl. Phys. Lett.*, 2005, **86**, 121101.

10 X. Liao, X. Yang, R. Zhang, J. Cheng, J. Li, S. Chen, J. Zhu and L. Li, *J. Mater. Chem. C*, 2017, **5**, 10001.

11 (a) Y.-T. Lee, Y.-T. Chang, C.-T. Chen and C.-T. Chen, *J. Mater. Chem. C*, 2016, **4**, 7020; (b) X. Liao, X. Yang, J. Cheng, Y. Li, X. Meng, J. Li, Q. Pei and L. Li, *ChemPlusChem*, 2018, **83**, 274.

12 (a) D. Zhang, D. Zhang and L. Duan, *ACS Appl. Mater. Interfaces*, 2016, **8**, 23197; (b) Z. Wang, H. Zhang, Z. Wang, B. Zhao, L. Chen, J. Li, H. Wang, Y. Hao and W. Li, *Org. Electron.*, 2018, **57**, 311; (c) D. Zhang, M. Cai, Y. Zhang, D. Zhang and L. Duan, *ACS Appl. Mater. Interfaces*, 2015, **7**, 28693; (d) C. Shi, N. Sun, Z. Wu, J. Chen, T. Ahamad, S. M. Alshehri and D. Ma, *Appl. Phys. Lett.*, 2018, **112**, 023301; (e) Y. Miao, B. Zhao, Z. Gao, H. Shi, P. Tao, Y. Wu, K. Wang, H. Wang, B. Xu and F. Zhu, *Org. Electron.*, 2017, **42**, 1; (f) Y. Miao, K. Wang, B. Zhao, L. Gao, P. Tao, X. Liu, Y. Hao, H. Wang, B. Xu and F. Zhu, *Nanophotonics*, 2018, **7**, 295.

13 (a) X.-K. Liu, C.-J. Zheng, M.-F. Lo, J. Xiao, Z. Chen, C.-L. Liu, C.-S. Lee, M.-K. Fung and X.-H. Zhang, *Chem. Mater.*, 2013, **25**, 4454; (b) X. K. Liu, W. Chen, H. Thachoth Chandran, J. Qing, Z. Chen, X. H. Zhang and C. S. Lee, *ACS Appl. Mater. Interfaces*, 2016, **8**, 26135; (c) B. S. Kim, K. S. Yook and J. Y. Lee, *Sci. Rep.*, 2014, **4**, 6019; (d) Z. Chen, X.-K. Liu, C.-J. Zheng, J. Ye, X.-Y. Li, F. Li, X.-M. Ou and X.-H. Zhang, *J. Mater. Chem. C*, 2015, **3**, 4283.

14 (a) Q. S. Zhang, B. Li, S. P. Huang, H. Nomura, H. Tanaka and C. Adachi, *Nat. Photonics*, 2014, **8**, 326; (b) H. Uoyama, K. Goushi, K. Shizu, H. Nomura and C. Adachi, *Nature*, 2012, **492**, 234; (c) Y. Suzuki, Q. Zhang and C. Adachi, *J. Mater. Chem. C*, 2015, **3**, 1700; (d) T. J. Penfold, F. B. Dias and A. P. Monkman, *Chem. Commun.*, 2018, **54**, 3926.

15 (a) Y. J. Cho, Y. Zhang, H. Yu and H. Aziz, *Adv. Funct. Mater.*, 2016, **26**, 8662; (b) Y. J. Cho, S. Taylor and H. Aziz, *ACS Appl. Mater. Interfaces*, 2017, **9**, 40564; (c) H. Li, Y. Tao, R. Chen,

G. Xie, C. Zheng and W. Huang, *J. Mater. Chem. C*, 2017, **5**, 4442.

16 X. Ban, W. Jiang, T. Lu, X. Jing, Q. Tang, S. Huang, K. Sun, B. Huang, B. Lin and Y. Sun, *J. Mater. Chem. C*, 2016, **4**, 8810.

17 J. Ye, C. J. Zheng, X. M. Ou, X. H. Zhang, M. K. Fung and C. S. Lee, *Adv. Mater.*, 2012, **24**, 3410.

18 J. Y. Wu and S. A. Chen, *ACS Appl. Mater. Interfaces*, 2018, **10**, 4851.

19 J. Sun, T. Zhang, X. Liao, K. Wang, M. Hou, D. Wu, Y. Miao, H. Wang and B. Xu, *Tetrahedron*, 2018, **74**, 1053.